Geochemistry Geophysics Geosystems G3

Published by AGU and the Geochemical Society

Article
Volume 13, Number 7
7 July 2012
Q07001, doi:10.1029/2012GC004033
ISSN: 1525-2027

Seismic imaging of the Cocos plate subduction zone system in central Mexico

YoungHee Kim
Lamont-Doherty Earth Observatory of Columbia University, 61 Route 9W, Palisades, New York 10964, USA (ykim@ldeo.columbia.edu)

Meghan S. Miller
Department of Earth Sciences, University of Southern California, Los Angeles, California 90033, USA (msmiller@usc.edu)

Frederick Pearce
Earth, Atmospheric and Planetary Sciences, Massachusetts Institute of Technology, Cambridge, Massachusetts 02139, USA (fpearce@mit.edu)

Robert W. Clayton
Seismological Laboratory, Division of Geological and Planetary Science, California Institute of Technology, Pasadena, California 91125, USA (clay@gps.caltech.edu)

[1] Broadband data from the Meso-America Subduction Experiment (MASE) line in central Mexico were used to image the subducted Cocos plate and the overriding continental lithosphere beneath central Mexico using a generalized radon transform based migration. Our images provide insight into the process of subducting relatively young oceanic lithosphere and its complex geometry beneath continental North America. The converted and reverberated phase image shows complete horizontal tectonic underplating of the Cocos oceanic lithosphere beneath the North American continental lithosphere, with a clear image of a very thin low-velocity oceanic crust (7–8 km) which dips at 15–20 degrees at Acapulco then flattens approximately 300 km from the Middle America Trench. Farther inland the slab then appears to abruptly change from nearly horizontal to a steeply dipping geometry of approximately 75 degrees underneath the Trans-Mexican Volcanic Belt (TMVB). Where the slab bends underneath the TMVB, the migrated image depicts the transition from subducted oceanic Moho to continental Moho at ~230 km from the coast, neither of which were clearly resolved in previous seismic images. The deeper seismic structure beneath the TMVB shows a prominent negative discontinuity (fast-to-slow) at ~65–75 km within the upper mantle. This feature, which spans horizontally beneath the arc (~100 km), may delineate the top of a layer of ponded partial melt.

Components: 10,800 words, 6 figures, 1 table.

Keywords: Mexico; inversion; mantle wedge; oceanic crust; subduction zone; volcanic arc.

Index Terms: 7220 Seismology: Oceanic crust; 8170 Tectonophysics: Subduction zone processes (1031, 3060, 3613, 8413); 8185 Tectonophysics: Volcanic arcs.

Received 9 January 2012; **Revised** 29 May 2012; **Accepted** 4 June 2012; **Published** 7 July 2012.

Kim, Y., M. S. Miller, F. Pearce, and R. W. Clayton (2012), Seismic imaging of the Cocos plate subduction zone system in central Mexico, *Geochem. Geophys. Geosyst.*, *13*, Q07001, doi:10.1029/2012GC004033.

1. Introduction

[2] The Mexican subduction zone is an ideal location to study subduction system dynamics because of significant variation in slab geometry along strike from northeast to southwest. The shallow subduction has been previously suggested between ~101°W and 96°W based on the relocated seismicity [*Pardo and Suárez*, 1995]. The Meso-America Subduction Experiment (MASE) experiment was designed to focus on the dynamics of the young Cocos plate, shallowly subducting beneath central Mexico. It is a multidisciplinary and multi-institutional project, which targeted to first determine the geometry and velocity structures of the downgoing plate, in particular, their relation to mineral and fluid-phase reactions in the subducting crust and mantle wedge, and second, to construct a geodynamical model of the subduction process. The data collecting stage of MASE provided two years (03/2005–02/2007) of broadband teleseismic and local data along a 550 km transect consisting of 100 sites with 6 ± 2 km station spacing (Figure 1). The transect is oriented nearly perpendicular to the Middle America Trench and spans from Acapulco on the Pacific side, through Mexico City, almost to Tampico, 100 km from the Caribbean coast (Figure 1).

1.1. Tectonic Setting

[3] The Cocos plate has been subducting underneath the North American plate for about 16 Ma [*Pardo and Suárez*, 1995] since it became detached from the Farallon plate at about 25 Ma [*Wortel and Cloetingh*, 1981; *Lonsdale*, 2005]. A distinct surficial manifestation from the Cocos plate subduction is the Trans-Mexican Volcanic Belt (TMVB, Figure 1), which consists of Neogene age arc volcanoes built on the southern edge of the North American plate [*Ferrari et al.*, 1999, 2011]. Along the MASE transect, the volcanic arc is about 300 km from the trench, which indicates subduction is presently quite shallow in comparison to most continental arcs. A systematic reorientation of a north-northwest-trending arc of the Sierra Madre Occidental (Figure 1) to the east-west-trending TMVB from 38 Ma to 7 Ma along with a change in the dominant composition of products from silicic ignimbrites and rhyolites to andesitic and basaltic lavas indicates changing conditions of slab dynamics [*Ferrari et al.*, 1999, 2011]. This transition may be related to the Miocene reorganization of the subducting slab beneath central Mexico [*Ferrari et al.*, 1999, 2011]. Magmatic activities ceased at 30 Ma along the coast and reappeared at 20 Ma just south of Mexico City and proceeded to migrate to the northern end of the TMVB [*Ferrari*, 2004; *Ferrari et al.*, 2011]. This may be indicative of slab flattening similar to what is observed and inferred in the western United States during the Laramide [*Humphreys et al.*, 2003; *Humphreys*, 2009] and more recently in northern Chile [*Kay and Mpodozis*, 2002, and references therein]. After this jump inland, it has been suggested that the slab in central Mexico has been rolling back, as evidenced by the southward migration of the TMVB volcanism, to its current location at the south edge of the TMVB [*Ferrari*, 2004; *Ferrari et al.*, 2011]. One of the puzzling aspects of the TMVB volcanism is that compositionally contrasting suites of rocks have erupted all across the arc since the middle-late Miocene [*Wallace and Carmichael*, 1999; *Schaaf et al.*, 2005; *Gómez-Tuena et al.*, 2007, 2008; *Straub et al.*, 2008, 2011]. Their proximity in location (along the arc front, a point 40 km south of the Mexico City where the MASE line crosses) indicates that these magmas must originate from separate, compositionally distinct domains in the subarc mantle [*Straub et al.*, 2011].

[4] The origin of the flat subduction in central Mexico is not apparent. It has been proposed that the flat or shallow subduction was formed primarily by the buoyancy of thickened oceanic crust in a form of an aseismic ridge or plateau and a delay in the basalt to eclogite transition due to the cool thermal structure of the overlying plate [*Gutscher et al.*, 2000]. *Skinner and Clayton* [2010] evaluated such previously proposed hypotheses for the case in Mexico, and suggested no obvious oceanic impactors that can explain current slab geometry except a change in the dynamics of subduction through a change in mantle wedge viscosity, possibly caused by water brought in by the slab. This is based on the numerical tests done by *Manea and Gurnis* [2007], which demonstrated that the subducted slab flattens as a consequence of suction forces acting on both subducting and overriding plates in response to the change in the viscosity and thickness of the mantle wedge. Narrowing the wedge in response to increased viscosity in the wedge and suction forces may be responsible for generating the flat slab subduction by preventing sinking of the oceanic plate into mantle in central Mexico [*Manea and Gurnis*, 2007].

[5] Another unusual aspect about the central Mexican subduction zone is the occurrence of the slow-slip events (SSEs) and nonvolcanic tremors (NVTs). Recent studies of episodic tremor and slip

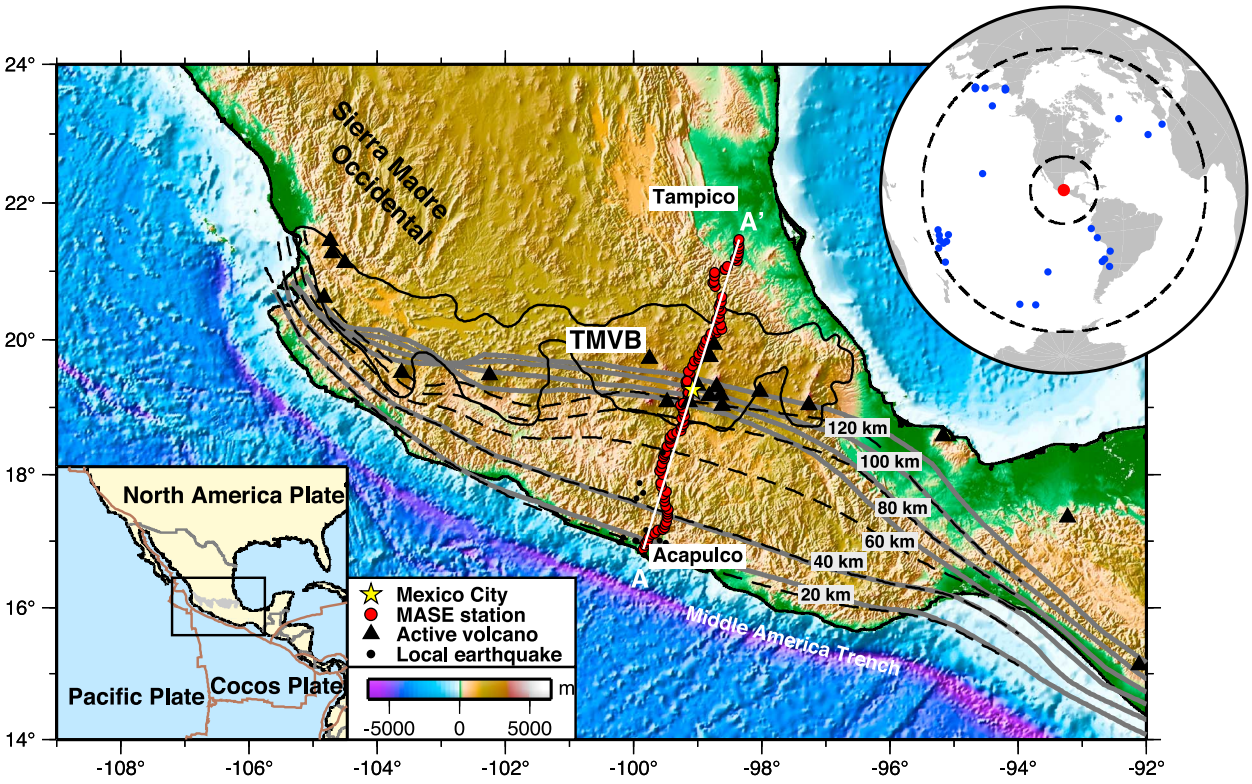

Figure 1. Topographic-bathymetric map showing the region of the study and stations. Lower-left inset illustrates regional tectonic framework, and upper-right inset teleseismic earthquake locations (shown as blue dots) used in the analysis. Seismic stations from the MASE are displayed in red circles, and active volcanoes are in black triangles. Local seismicity (event-station distance < ~50 km) is shown as black dots. The area enclosed by a black solid line indicates Quaternary volcanic area known as Trans-Mexican Volcanic Belt (TMVB). Gray solid contour lines represent the isodepth contours of the subducted Cocos slab in 20 km depth interval, constrained by local seismicity and receiver functions [*Pérez-Campos et al.*, 2008; *Kim et al.*, 2010]. Dashed contour lines for 20 to 100 km depth are from *Pardo and Suárez* [1995] based on relocated seismicity. The surface projection of the seismic profile (16 degrees from the north) is shown by line A-A′.

(ETS) in both Cascadia and Japan point to an origin that involves fluids near the plate boundary [i.e., *Kodaira et al.*, 2004; *Audet et al.*, 2009; *Rubinstein et al.*, 2010]. In central Mexico, the NVT locations coincide with the place within and above the subducting oceanic crust where the fluid content has been suggested to be high [*Kim et al.*, 2010]. Slow slip patches coincide with the very low velocity layer near the top of the subducted oceanic crust [*Song et al.*, 2009; *Song and Kim*, 2012b].

1.2. Slab Morphology

[6] *Pardo and Suárez* [1995] first described the shallow slab subduction beneath central Mexico based on relocated hypocenters of local earthquakes (see dashed lines for contour and dots for selected seismicity in Figure 1). More accurate along-strike slab geometries were obtained using teleseismic converted phases recorded from the seismic lines in Mexico [*Pérez-Campos et al.*, 2008; *Melgar and Pérez-Campos*, 2011; *Kim et al.*, 2010, 2011; *Song and Kim*, 2012a, 2012b] (see gray lines in Figure 1) and tomography [*Husker and Davis*, 2009; T. Chen and R. W. Clayton, Structure of central and southern Mexico from velocity and attenuation tomography, manuscript submitted to *Journal of Geophysical Research*, 2012]. In particular, *Pérez-Campos et al.* [2008] presented the receiver function (RF) image showing, for the first time, the Cocos slab in central Mexico horizontally underplating the base of the continental crust with no room for asthenosphere for approximately 300 km from the Middle America Trench. Of the flat subduction regions, the subduction system in central Mexico is unique in a sense that the horizontal oceanic crust with normal oceanic crustal thickness of 6–8 km is situated at a very shallow depth (~45 km) [*Pérez-Campos et al.*, 2008; *Kim et al.*, 2010]. Since there is very little intermediate

to deep seismicity away from the seismogenic zone adjacent to the trench, there has been no consensus model of the slab geometry farther to the north of this region, specifically underneath the TMVB. P wave tomography [*Gorbatov and Fukao*, 2005] suggested the slab dips very steeply (~90 degrees) beneath the TMVB, and more recent results using the MASE data set imaged the Cocos plate underneath the TMVB subducting at approximately 75 degrees [*Husker and Davis*, 2009].

[7] The complex geometry and unusual properties of the subduction zone system beneath central Mexico have made previous efforts to image the slab morphology challenging, especially the transition from horizontal to steeply dipping. In this study, we use scattered waves within the P wave coda of teleseismic events to image the lithospheric structure down to a depth of 150 km in order to clarify the slab geometry and inferred relationships to the overriding plate, volcanic arc processes, seismicity, and overall plate boundary evolution.

2. Data and Methods

[8] As earthquake body waves travel through the Earth, they produce a sequence of reflections, refractions, and conversions at discontinuities separating regions of differing seismic impedance. The task of seismic imaging is to identify the location and magnitude of these seismic discontinuities from surface recording of such scattered waves. Since we have a dense linear seismic array (6 km interstation spacing on average), it is amenable to higher-resolution seismic migration techniques and can provide images with much more detail than those previously obtained. The imaging method used in this study is based on the scattering theory, so does not assume planar boundaries of the incident wavefield [*Bostock et al.*, 2001] compared to teleseismic RF method where planar and horizontal boundaries are assumed [*Langston*, 1979].

2.1. Teleseismic Migration

[9] The 2-D generalized radon transform-based migration (hereafter 2-D GRT) method used in this study inverts scattered waves within the teleseismic P wave coda for sharp variations in the Earth's elastic properties beneath a densely spaced station array [*Bostock and Rondenay*, 1999; *Bostock et al.*, 2001; *Rondenay et al.*, 2005; *Rondenay*, 2009]. This method has been extensively applied to array data sets in other subduction zones (e.g., Alaska [*Rondenay et al.*, 2008, 2010], Cascadia [*Bostock et al.*, 2001; *Abers et al.*, 2009], Costa Rica and Nicaragua [*MacKenzie et al.*, 2010], and western Hellenic [*Suckale et al.*, 2009; *Pearce et al.*, 2012]). The inverse problem can be viewed as a weighted diffraction stack over all sources and receivers that yields an estimate of the scattering potential at a given point in the subsurface [*Bostock and Rondenay*, 1999; *Bostock et al.*, 2001; *Rondenay et al.*, 2005]. The scattering potential is then linearly inverted for velocity perturbations at each point [*Rondenay et al.*, 2005] and the inverse problem is solved for all points in model space to obtain a 2-D image of velocity perturbations.

[10] The method involves two steps: (1) the recorded data is preprocessed to isolate the scattered wavefield [*Bostock and Rondenay*, 1999] and (2) the 2-D GRT method is applied to produce an image of velocity perturbations. The description of the preprocessing procedure has been described in previous papers [*Rondenay et al.*, 2001; *MacKenzie et al.*, 2010; *Pearce et al.*, 2012]. We note that we used the preprocessing step further improved by *Pearce et al.* [2012], and the modifications are briefly highlighted here. First, longer source time functions (up to ~180 s) are used to make sure that source-side scattering is included in the estimate of the incident wavefield. Second, the scattered wavefield is precisely aligned to the incident P wave using several iterations over the following steps: (1) align the incident wavefield using multichannel cross-correlation [*VanDecar and Crosson*, 1990], (2) estimate the source time function from the 1st principal component of the aligned P wavefield [*Ulrych et al.*, 1999], and (3) deconvolve the incident wavefield from each scattered wavefield component. Third, an optimal damping parameter (water level) in the deconvolution is estimated for each station component as opposed to using a uniform damping value.

[11] The 2-D GRT method assumes that the scattered wavefield is generated by volumetric perturbations in P and S wave velocities within a smoothly varying background velocity model. The 1-D reference model used in this study is described in section 2.2. The 2-D GRT simultaneously inverts a combination of forward and backscattered (or reverberated) modes using analytical expressions for their traveltimes and amplitudes. The scattering modes used in this study are illustrated in Figure 2a. They are defined as the incident *P*-wave forward scattered as an *S*-wave (Pds); the free-surface-reflected *P*-wave backscattered as a *P*-wave (Ppdp); the free-surface-reflected *P*-wave backscattered as an *S*-wave

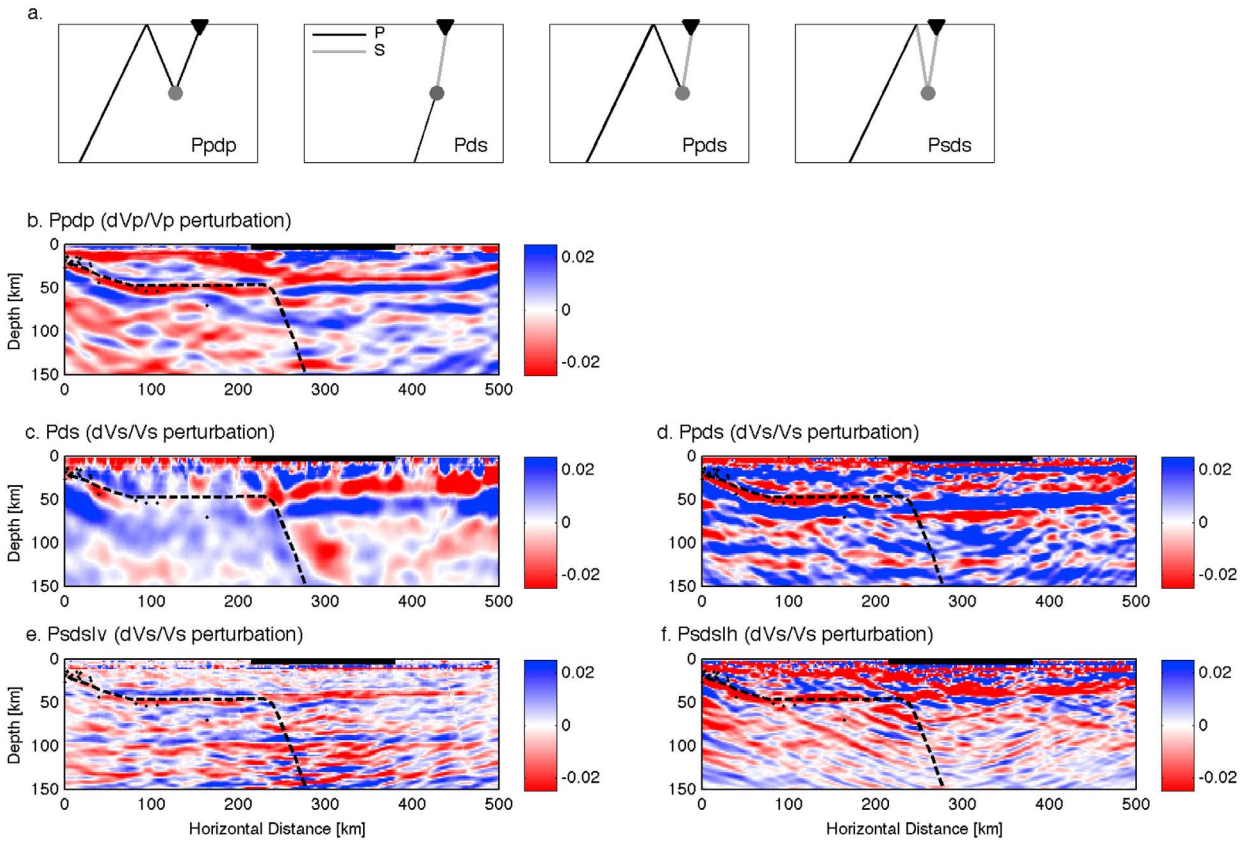

Figure 2. Images showing individual mode contributions. (a) Schematic raypath diagram showing individual seismic modes. (b–f) Contributions from each scattering modes for one forward mode (Pds) and four backscattered modes (Ppdp, Ppds, Psds|v, and Psds|h), showing the 500 km transect (A-A′ in Figure 1) across central Mexico. Red to blue color scale represents negative (slower) to positive (faster) P wave and S-wave velocity perturbations relative to our merged one-dimensional background model using [*Valdes-Gonzalez and Meyer*, 1996] and IASP91 for depths greater than 45 km [*Kennett and Engdahl*, 1991] (Table 1). Each panel includes interpreted profiles with the top interface of the subducted Cocos plate [*Pérez-Campos et al.*, 2008; *Kim et al.*, 2010] as dashed lines and relocated seismicity [*Pardo and Suárez*, 1995] as dots. The arc location is shown as a black line at 0 km depth, horizontally spanning from 220 and 380 km.

(Ppds); and the free-surface-reflected *S*-wave backscattered as an *Sv*-wave (Psds|v) and *Sh*-wave (Psds|h). Only the Ppdp mode has sensitivity to P wave velocity perturbations (hereafter dVp/Vp). The four remaining scattering modes are sensitive to S-wave velocity perturbations (hereafter dVs/Vs image) and are combined to form a single composite image using the approach of *Rondenay et al.* [2001].

[12] The resolution of the 2-D GRT has been shown to depend largely on the frequency content of the scattered signal and the source/receiver distribution as has been documented in numerous previous studies [*Bostock et al.*, 2001; *Shragge et al.*, 2001; *Rondenay et al.*, 2005; *Rondenay*, 2009]. In general, each scattering mode has a different ability to resolve the location, volume, and dip of subsurface structures as described by the spatial gradient of its total travel time function (see *Rondenay et al.* [2005] for details). Forward scattered waves generally provide comprehensive dip resolution, particularly for near-vertical structures, but their volume resolution is 3–5 times lower than backscattered waves. However, backscattered waves have limited dip resolution, particularly at dips greater than 50°. Given the frequency content of the scattered signals used here (<0.3 Hz), we expect backscattered waves to have a volume resolution of ∼3 km for modestly dipping structures in the lower crust and upper mantle.

[13] The Cocos slab underneath the arc in central Mexico has steep geometry [*Husker and Davis*, 2009], which has made it difficult to image with the lack of deep seismicity. However, we adapted

Table 1. One-Dimensional Reference Model

Layer	Depth Ranges (km)	Vp (km/s)	Vs (km/s)	Density (g/cm^3)
1	0–10	5.8	3.3	2.7
2	10–20	6.6	3.8	2.9
3	20–30	7.2	3.9	3.0
4	30–40	7.5	4.2	3.0
5	40–60	8.0	4.4	3.2
6	60–550	8.3	4.5	3.3

the methodology described in *MacKenzie et al.* [2010], who primarily used upgoing Pds scattered waves to image the steeply subducting (>60 degrees) slab in Central America. They found reverberations at the steep interface do not reach the stations and we also note in individual mode contribution images (Figure 2) that the reverberated phases, except for the direct Pds mode, do not show the conversion at the steeply dipping interface. Therefore, we employ a depth-dependent weighting scheme to enhance the contribution from the Pds mode at the depth greater than 60 km in stacking the individual scattering mode contributions.

2.2. Data

[14] In this study, we use teleseismic earthquake sources occurring over a wide azimuthal distribution to illuminate the sub-array structure. The selection of events are based on four sets of criteria: (1) occur within epicentral distances from 30 to 90 degrees from the MASE array; (2) have a magnitude (m_b) greater than 6.0; (3) have an incident P wave arrival that can be identified across the array; (4) have no contamination with other arrivals from foreshocks, aftershocks, or secondary phases (i.e., PcP, PP). In order to avoid biases in backazimuthal coverage, we tighten the selection criteria for active regions such as Tonga-Fiji and South America and use only a subset of the events with high signal-to-noise ratio, which were recorded at a majority of the stations. For regions that had fewer events, we reduce the minimum magnitude requirement to m_b = 5.5 and used shallow-depth events (<10 km). By tightening and loosening these criteria similar to those by *Pearce et al.* [2012], the resulting data set consist of 30 high-quality earthquakes (Figures 1 (inset), 3 and 4).

[15] The background reference model is essential for obtaining robust images from the 2-D GRT method [*Rondenay*, 2009]. We use a composite 1-D velocity model based on a previous local velocity model [*Suarez et al.*, 1992; *Valdes-Gonzalez and Meyer*, 1996] and a global IASP91 model [*Kennett and Engdahl*, 1991] for depths greater than 45 km (Table 1). It is also consistent with the velocity model used in the relocation of local seismicity [*Pardo and Suárez*, 1995] as shown in Figures 2, 5, and 6. These local earthquakes are selected from epicenters within 50 km of the MASE line (Figure 1), and projected on an optimal projection azimuth of 16 degrees (see a profile A-A′ in Figure 1). This azimuth is perpendicular to the trench and also indicates the slab's steepest descent.

3. Results

[16] Here we present 2-D GRT images along the Cocos plate subduction system. The migration constrains depths to major boundaries such as the top of the subducting slab and the oceanic crust/continental crust-mantle interface of the slab. Resulting both P wave and S-wave velocity perturbation profiles across A-A′ (Figure 1) with red to blue color scale represent negative (slower) to positive (faster) velocity perturbations with respect to the 1-D reference model (Table 1). Velocity discontinuities are thus denoted by color contrasts (i.e., red-to-blue or blue-to-red) [*Rondenay et al.*, 2005].

[17] We test the ability of migration from synthetic seismograms based on the ray-based algorithm [*Frederiksen and Bostock*, 2000] to directly compare with the images from the actual data (see section 3.1). We also test the sensitivity in our image quality by using different event distributions, background velocities, and projection angles (see section 3.2).

3.1. Synthetic Test to Image the Steep Slab

[18] As discussed in detail by *MacKenzie et al.* [2010], it is challenging to image a steeply dipping structure from a linear station array geometry because the steep dip (>50 degrees) causes converted phases to travel over larger lateral offsets. Thus, only a contribution from the upgoing Pds phase has a capability to image the steep slab [*MacKenzie et al.*, 2010]. We follow a synthetic set-up similar to the one as demonstrated in *MacKenzie et al.* [2010] to examine the ability of migration from synthetic seismograms for imaging the steeply dipping interface.

[19] The synthetics [*Frederiksen and Bostock*, 2000] are calculated from (1) a model with a

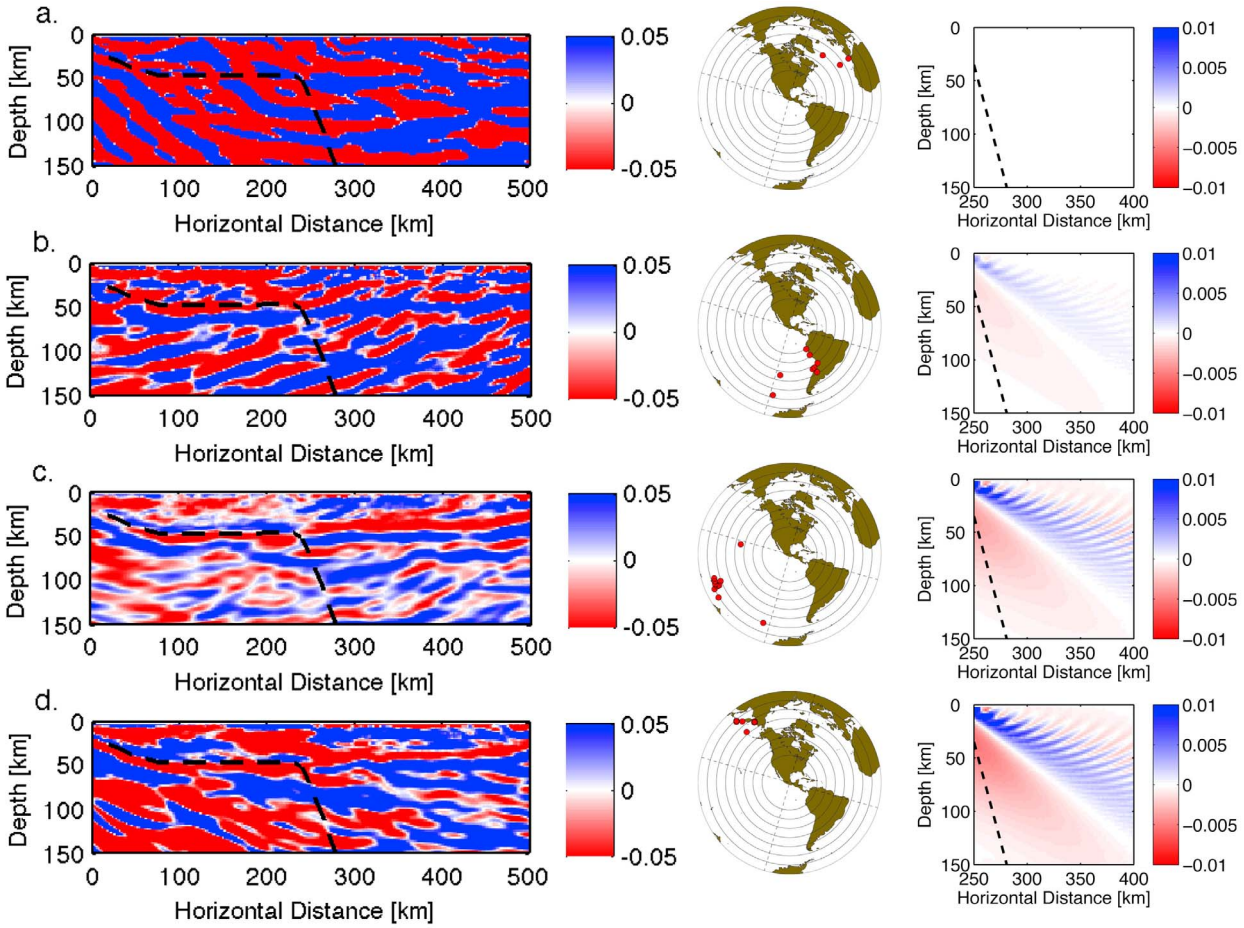

Figure 3. Azimuthal contributions to the dVp/Vp images based on both data (left) and synthetic seismograms (right) from the event distribution (middle). Quadrants are defined relative to the azimuth of maximum slab dip. The synthetic seismograms [*Frederiksen and Bostock*, 2000] are generated in a model with a dipping layer with a slope of 75 degrees. (a) Images from the quadrant 1 (3 events). (b) Images from the quadrant 2 (8 events). (c) Images from the quadrant 4 (10 events). (d) Images from the quadrant 4 (9 events). The dashed line in the dVp/Vp image from the data (left) indicates the top interface of the subducted Cocos plate [*Pérez-Campos et al.*, 2008; *Kim et al.*, 2010]. The dashed line in the dVp/Vp image from the synthetics (right) indicates the steep interface with the dip of 75 degrees.

dipping structure with a slope of 75 degrees and receivers with interstation distance of 10 km, and (2) the same earthquake locations as the actual data (Figure 1, inset). Then, they are migrated in the same manner as the actual data. Individual model contributions are shown in Figure S1 in the auxiliary material, and shows that only the Pds mode produces conversions at the steeply dipping interface.[1] As also shown in *MacKenzie et al.* [2010], the images from Ppds and Psds modes include a "ghost" of the Pds conversion at both shallower depths and dips (Figure S1). This is due to the incomplete sampling in ray angle [*MacKenzie et al.*, 2010]. In addition, the effect of the depth-dependent weight on the Pds mode is tested and shown in Figure S2. The image below 60 km depth with the depth-dependent weight is mostly controlled by the Pds mode, and this additional depth-dependent weighting scheme clearly improves the image of the steeply subducting slab underneath the arc (Figure S2).

3.2. Sensitivity to a Range of Backazimuth, Background Velocity, and Projection Line

[20] Figures 3 and 4 show azimuthal contributions to the dVp/Vp and composite dVs/Vs images, respectively. The teleseismic events (Figure 1, inset) are divided in four quadrants, which are defined relative to the azimuth of maximum slab dip [see, e.g., *Rondenay et al.*, 2010]. In these figures, we

[1]Auxiliary materials are available in the HTML. doi:10.1029/2012GC004033.

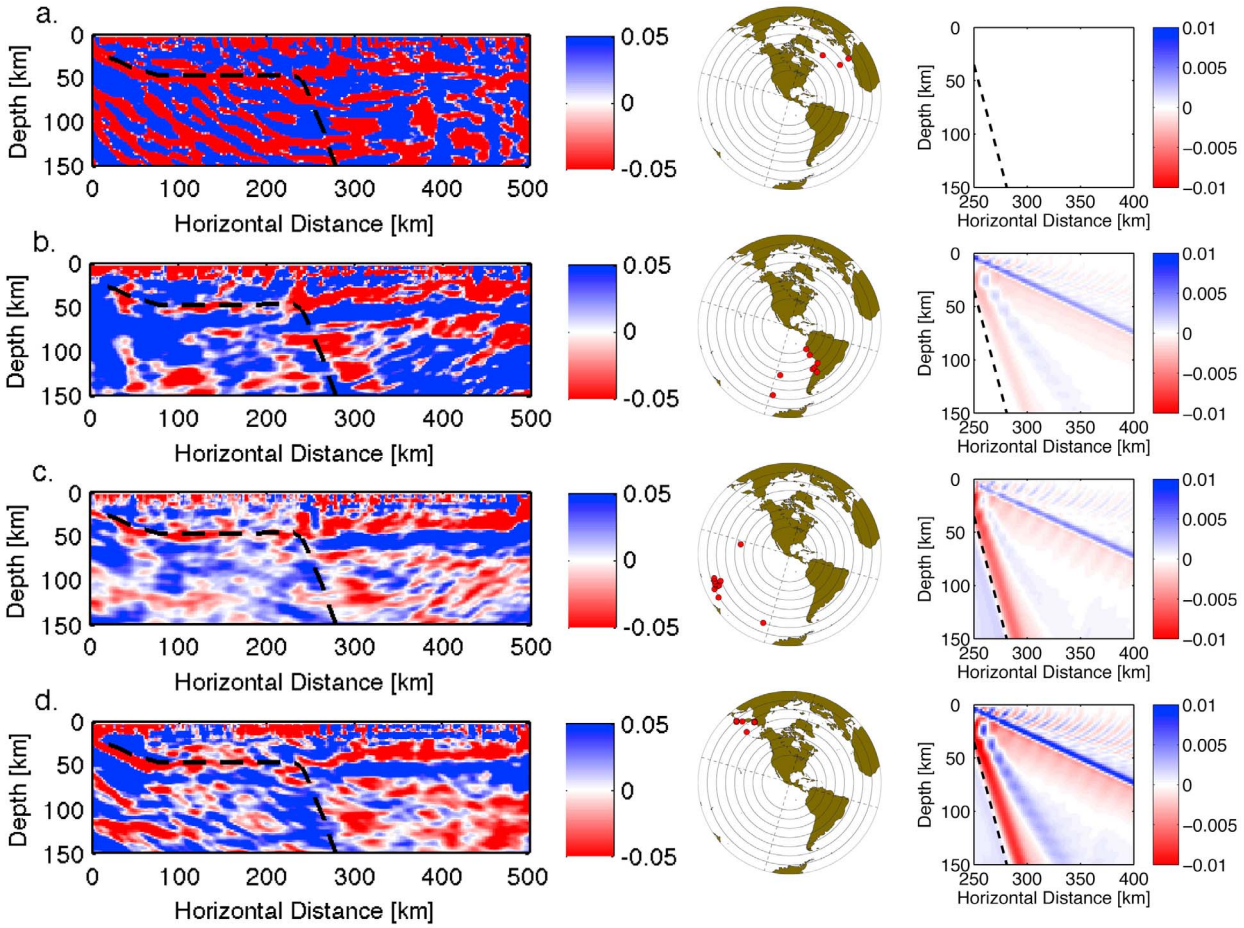

Figure 4. Azimuthal contributions to the dVs/Vs images based on both data (left) and synthetic seismograms (right) from the event distribution (middle). Quadrants are defined relative to the azimuth of maximum slab dip. The synthetic seismograms [*Frederiksen and Bostock*, 2000] are generated in a model with a dipping layer with a slope of 75 degrees. (a) Images from the quadrant 1 (3 events). (b) Images from the quadrant 2 (8 events). (c) Images from the quadrant 4 (10 events). (d) Images from the quadrant 4 (9 events). The dashed line in the dVs/Vs image from the data (left) indicates the top interface of the subducted Cocos plate [*Pérez-Campos et al.*, 2008; *Kim et al.*, 2010]. The dashed line in the dVs/Vs image from the synthetics (right) indicates the steep interface with the dip of 75 degrees. We note that there is no depth-dependent weight applied in the images shown.

also show the migrated images from the synthetic seismograms generated by the same set-up described in section 3.1, but using the events in each quadrant. Figures 3 and 4 demonstrate that the method requires quality events in good azimuthal distribution, and also requires the incident wavefields coming from the quadrants 3 and 4 (Figures 3c, 3d, 4c, and 4d) to better recover the overall structure. Also, Figures 3 and 4 demonstrate that the subducted shallow-to-flat oceanic crust and the Moho of the overriding plate are robust features that can be seen from the all the quadrants. In particular, Figure 4 shows that the earthquakes from south or rays, which obliquely incident to the 2-D station array, are required to image the steeply dipping structure.

[21] In addition to our merged 1-D background model, we use two different background models, such as a global IASP91 model (Table S1 in Text S2) or a two-layer model (Table S2 in Text S2), to test the sensitivity of the resulting images to the different background models. We find that using different background models has overall minimal influence on the location and coherence of imaged structures (Figure S3). However, the merged 1-D background model resolves the depth and dip of the top interface of the subducted oceanic crust, which are fully consistent with previous RF analysis [*Kim et al.*, 2010] (Figure S3). Nevertheless, the same background model is used for both the migration and hypocenter relocation to minimize the source of bias when

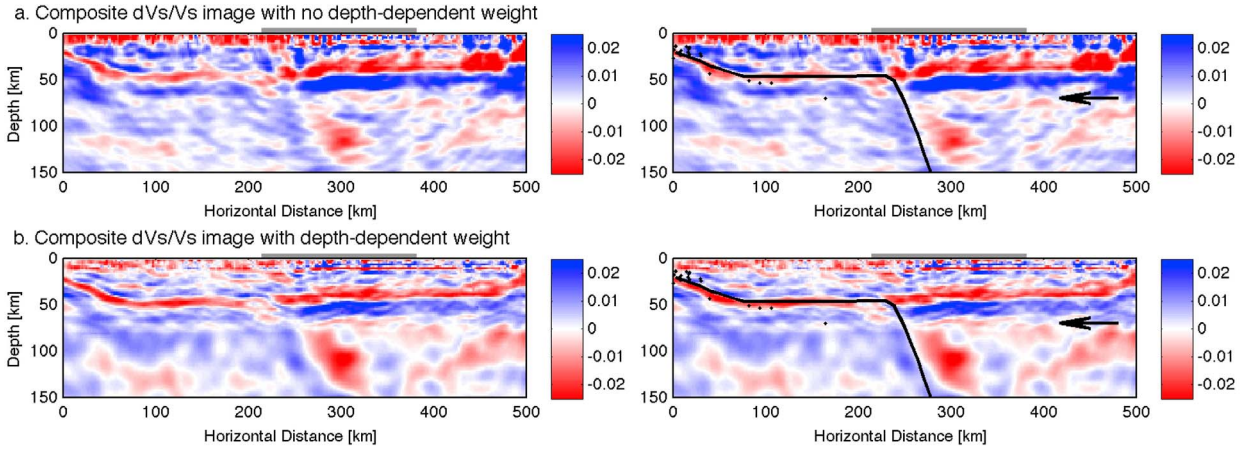

Figure 5. Composite dVs/Vs images showing the 500 km transect (A-A′ in Figure 1) across central Mexico (left: uninterpreted, right: interpreted). (a) Image with no depth-dependent weight. Individual mode shown in Figure 2 are stacked together to form the images with the weight, $w_1 = 5$ for Pds, $w_2 = 3$ for Ppds, $w_3 = 0.5$ for Psds|v and $w_4 = 0.5$ for Psds|h, based on the rationale developed in *Rondenay et al.* [2001]. (b) Image with the depth-dependent weight on the Pds phase for depth greater than 60 km in addition to the above mentioned weights. Note that structure, especially at shallow depth (∼40–50 km) is better resolved with the depth-dependent weighting scheme. The arc location is shown as a gray line above each plot. The thin horizontal low-velocity feature at the depth of ∼70 km is indicated by an arrow, which is discussed in section 4.2.

comparing the location of imaged structures and seismicity.

[22] We also test a range of projection lines with 10° increments in azimuth (−6°, 6°, 16°, 26°, 36°, and 46°), and Figure S4 shows corresponding composite dVs/Vs images with no depth-dependent weight on the direct Pds phase. We find that the optimal projection azimuth is 16° ± 10°, and obtain the most focused signal from our imaging targets such as the low-velocity oceanic crust, the overriding Moho, and the steep interface beneath the arc (Figure S4). As the projection angle increases/decreases, away from the optimal azimuth, migration artifacts such as "migration smiles" appear due to insufficient spatial sampling in the northern region near the Caribbean coast.

3.3. Migrated Images

[23] As more migrated phases (Figure 2) are stacked in, we observe that the artifacts due to cross-mode contamination (i.e., parallel echoes of the real structure [*Rondenay*, 2009]) become attenuated while energy mapped to its correct depth is sharply imaged (Figures 5 and 6). Figures 2b–2f show individual mode contributions from forward-scattered (Pds) and backscattered phases (Ppdp, Ppds, Psds|v and Psds|h). The image from the Psds|v mode (Figure 2e) has smaller amplitudes compared to the images from other modes, and does not resolve shallowly dipping segments in both Pacific and Caribbean coast. According to *Rondenay* [2009], in general, the Psds|v mode image does not resolve the structure compared other seismic modes because all the teleseismic waves are obliquely incident to the seismic array and preferentially excite SH-to-SH backscattering. Also, we observe that the thin oceanic crust shown as low velocities is clearly imaged except from the direct Pds mode (Figure 2c). The Pds mode is not sensitive to horizontal features as demonstrated in *Rondenay* [2009] showing small total travel gradients for small or nearly horizontal dip of the structure [see *Rondenay*, 2009, Figure 16]. Also, the flat oceanic crust (∼75 km to 200 km laterally) is not clearly imaged possibly due to the lower frequency filter of 0.03–0.3 Hz in the migration (see *Kim et al.* [2010, Figure 10] for higher frequency version of the Pds mode). The continental Moho underneath the TMVB and the northern region are imaged consistently across the individual mode profiles.

[24] In this paper, we focus on the migrated image obtained from the stack of S-scattered waves (Figures 5 and 6) because it is based on larger number of scattered waves that afford greater volume and dip resolution, and the S-scattered waves are more accurately separated from the full wavefield than P waves [*Rondenay*, 2009]. Figure 5

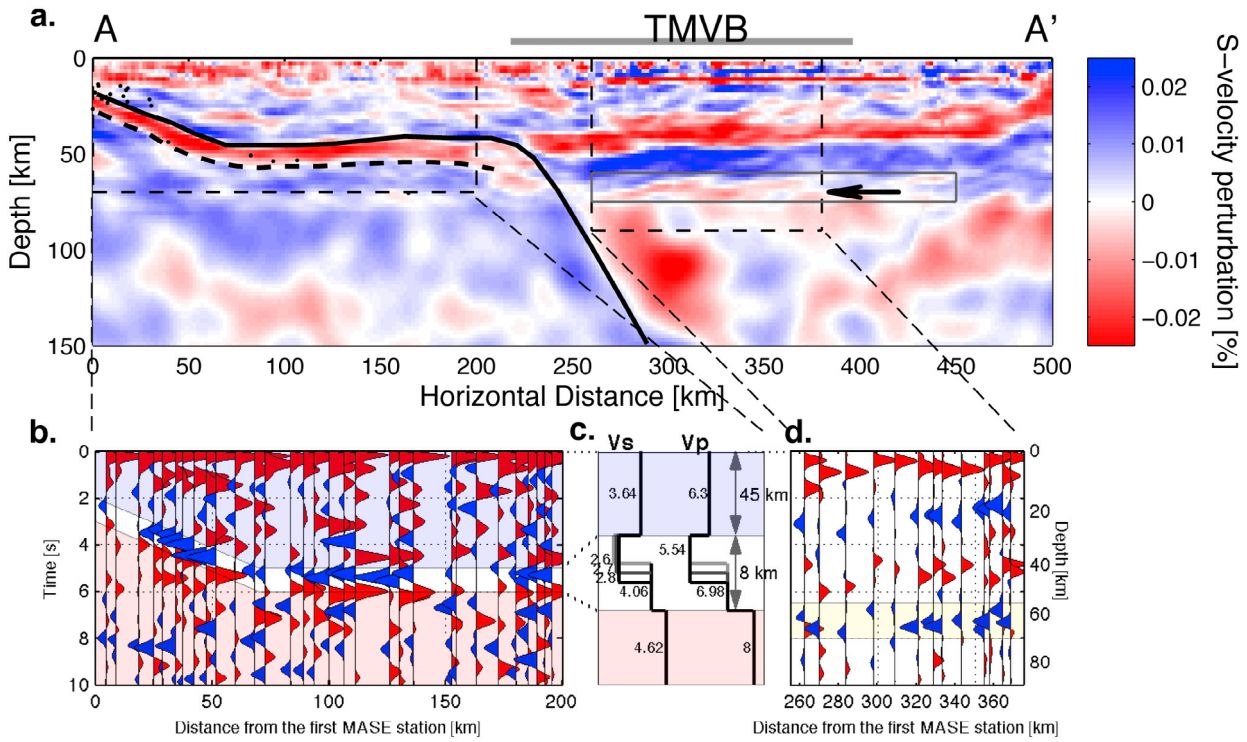

Figure 6. Seismic images showing a 500 km transect (A-A′ in Figure 1) across central Mexico. (a) Composite dVs/Vs image with the depth-dependent weighting scheme. The gray box includes the migration artifact due to cross-mode contamination. (b) Teleseismic receiver function (RF) cross section from Acapulco to the start of the TMVB, showing the shallow-to-flat oceanic crust. The single event that occurred on 21 March 2005 in Bolivia (south-east from the MASE) is first filtered at 0.01–1 Hz and processed by the time domain deconvolution [*Kikuchi and Kanamori*, 1982; *Ligorria and Ammon*, 1999] with a Gaussian filter parameter of 4. Blue color indicates the negative impedance contrast across the top of the subducting oceanic crust whereas red color the positive impedance contrast across the bottom of the subducted crust. Light blue, white, and light pink overlays denote the continental crust, oceanic crust, and oceanic lithosphere, respectively. (c) P wave and S-wave velocity models for the flat slab region down to a depth of 90 km with the same color scheme as the RF section on the left [*Kim et al.*, 2010]. We note that the anomalously low velocity feature in the subducting upper oceanic crust [*Song et al.*, 2009; *Kim et al.*, 2010] is not seen in the present data. (d) The RF cross section using stations above the TMVB and an event on 20 April 2006 near Kuril islands (north-east from the MASE) (see Figure S5). Seismograms are filtered at 0.03–0.5 Hz to suppress high noise level from the cultural noise and scattering by the volcanic rocks. Strong (negative) conversions at 6.5–8 s (65–75 km depth) after P arrival at 0 s are highlighted in yellow (and an arrow in the composite dVs/Vs image). Note that negative or positive peaks in the RFs indicate the locations of the discontinuity whereas crossovers between opposite polarity peaks mark the discontinuity in the migration. See auxiliary material for brief description of the RF method and how the waveforms are processed.

demonstrates the effect of the additional depth-dependent weight only on the Pds mode for the depth greater than 60 km. Images showing both the shallow-to-flat transition of the thin oceanic crust at the depth of ∼45–50 km and the steep subduction beneath the TMBV are further enhanced by this weight (Figure 5b).

[25] The images in Figure 6 show a strong slab signature in the top 60 km, which confirms the flat subduction of oceanic plate, all the way to the south of the TMVB. The dip and depth of the crust and Cocos slab are in good agreement with the previously published RF images [*Pérez-Campos et al.*, 2008; *Kim et al.*, 2010; *Song and Kim*, 2012a, 2012b], but the images provide much more detail about lithospheric structure of both the overriding and downgoing plates (Figure 6a). The subducting oceanic crust is revealed as a shallowly dipping low-velocity layer with a thickness of 7–8 km. It dips to the north at about 15 degrees for 80 km from the coast and then horizontally underplates the continental crust for 200 km. This portion, detailed in Figure 6b, shows a shallow-to-horizontal interface that has a distinct negative RF pulse over a positive one. The peak of the RF pulse indicates the discontinuity interface with its polarity controlled

by the impedance contrast across the discontinuity [*Langston*, 1979] whereas velocity discontinuities in the migrated images are shown by color contrasts. As also shown in Figure 6c, modeling of (1) the RF conversion amplitudes of the horizontal slab [*Kim et al.*, 2010], (2) locally observed converted SP arrivals [*Song et al.*, 2009], and (3) teleseismic underside reflections [*Song et al.*, 2009] reveal a thin (∼4 km) low-velocity (shear wave velocity of 2.6–2.8 km/s, which is ∼20−30% slower than normal oceanic crustal velocities) layer between the Cocos plate and the Paleozoic and Precambrian continental crust [*Jording et al.*, 2000].

[26] The crustal thickness between 75 km from the first station of MASE at Acapulco and the southern end of TMVB ranges from 45 to 50 km (Figure 6a), agreeing with previous seismic refraction data and gravimetric studies [*Valdes-Gonzalez and Meyer*, 1996; *Jording et al.*, 2000]. The section beneath the TMVB exhibits a relatively flat Moho topography (slightly varying in depth between 38 and 43 km) with no continental root associated with ∼2 km surface topography associated with the TMVB (Figure 6a). Strong velocity contrast between the lower continental crust and upper-most mantle wedge (Figure 6a) can be attributed high-attenuation lower crustal region [*Chen and Clayton*, 2009], which also correlates well with the low-resistivity [*Jording et al.*, 2000; *Jödicke et al.*, 2006] and low shear wave velocity region [*Iglesias et al.*, 2010]. Beyond the northern extent of the TMVB, the crustal thickness shallows to 35 to 25 km toward the end of the MASE array (Figure 6a). We note that the image does not extend to the end of the array (∼533 km) because the data are sparsely spaced closer to the end of the array as discussed in *Kim et al.* [2010] and thus the sharpness of the image suffers from not enough sampling.

[27] Figure 6a shows the relocated seismicity with $m_b > 4.5$ [*Pardo and Suárez*, 1995] mostly concentrated in the top of the shallowly dipping oceanic crust near Acapulco in the Pacific coast (Figure 1). Dominant interplate earthquake mechanisms are thrust, associated with the Cocos plate subduction in this region [*Pardo and Suárez*, 1995]. The image of the flat oceanic crust segment includes very little inslab seismicity, which does not extend beyond ∼120 km from the coast (Figure 6a). Also, no crustal seismicity is observed in the overriding plate over the subducted Cocos plate, which may suggest low couplings between two plates. Furthermore, there is complete absence of a Wadati-Benioff zone beneath the arc (Figure 6a), and so the geometry of the slab cannot be inferred from the seismicity.

[28] The image of the steeply plunging slab in the southern end of the TMVB is clearly recovered from the 2-D GRT method (Figure 6a), regardless of strong lateral velocity contrasts at the vicinity of the mantle wedge. Previous RF imaging of the section underneath the TMVB was less well determined compared to the region to the south due to complications in the seismic waveforms passing through the volcanic region and deep sedimentary Valley of Mexico basin [*Pérez-Campos et al.*, 2008; *Kim et al.*, 2010]. The slab appears to abruptly change from nearly horizontal to a steeply dipping geometry of approximately 75 degrees. The amplitude of the thin low-velocity oceanic crust decreases significantly where the slab bends at the southern end of the TMVB with a lateral extent of 200–245 km and a depth of 45–60 km (Figure 6a). Beyond 60 km depth, the top of the subducting oceanic crust can only be traced below the broadly diffused boundary (Figure 6a) similar to images of the Costa Rica slab [*MacKenzie et al.*, 2010] and migration of the synthetic seismograms (Figures 4, S1 and S2). The steep Cocos slab extends down to a depth of 200 km and its converted signal diminishes with increasing depth. For a fixed array width and complete range of teleseismic incidence angles, the resolution decreases with depth as the coverage in spatial gradient of the scattered lag time and the range in ray orientation, measured from a constant travel-time delay between the upcoming incident wave and the scattered wave, tend to diminish [*Rondenay et al.*, 2005; *Rondenay*, 2009]. Beneath the TMVB, we observe a negative discontinuity at 65–75 km depth (Figure 6a). We note that this feature is not so evident compared to the RF image (Figures 6d and S5), and also appears to continue to the north (Figure 6a) due to the cross-mode contamination, especially in the Ppds mode (Figure 2d). Based on the synthetic test, assuming that the Moho depth is 45 km underneath the arc, the parallel echo of this seismic discontinuity appears at the depth of ∼65 km.

4. Discussion

4.1. Subducted Oceanic Crust

[29] One unusual structural feature of the central Mexican subduction zone that was revealed by the MASE experiment is the presence of the thin low-velocity layer, which has been suggested as altered oceanic crust [*Kim et al.*, 2010; *Song and Kim*, 2012b]. According to *Manea and Gurnis* [2007], the low-velocity (or low-viscosity) layer above the subducted oceanic crust is needed in numerical models to sustain the flat slab geometry without

strong coupling between the overriding plate and the slab. The presence of such a layer in the subduction zone has previously been proposed for Japan [*Hirose and Obara*, 2005] based on the NVT observation, but in Central Mexico it is directly imaged as a shallowly dipping, 7–8 km thick, low-velocity oceanic crust directly beneath the North American plate without any mantle lithosphere above the subducted crust (Figure 6a). Although modeling of local converted S-to-P phase [*Song et al.*, 2009] and the RF amplitudes [*Kim et al.*, 2010] suggested the presence of anomalously low shear speeds (2.6–2.8 km/s) in the upper 3–4 km oceanic crust, in our image we only see intergraded low-velocity oceanic crust and do not observe significant velocity reduction in the upper oceanic crust because the underplated, extremely low-velocity feature is quite thin (Figure 6c). We note that such constrained velocities are far too low with respect to velocities obtained for unaltered MORB and gabbro over pressure of ~1 GPa and temperature ranges of 500–800°C [*Hacker et al.*, 2003]. In the Cascadia subduction zone, *Audet et al.* [2009] and *Peacock et al.* [2011] argued that their high Vp/Vs values of 2.35 ± 0.10 cannot be due to compositional effects (mineralogy within the downgoing oceanic crust) but the presence of near-lithostatic pore fluid pressures within the 5 km thick subducting Juan de Fuca crust. In central Mexico, the added pore pressure and the presence of hydrous minerals (such as talc) may possibly explain such low shear speeds in the shallow-to-horizontal part of the upper oceanic crust [*Kim et al.*, 2010; *Song and Kim*, 2012b]. In particular, the low velocity layer in the shallowly dipping segment near the Pacific coast (Figures 6a and 6b), which coincides with the transition downdip to the locked zone, can be characterized by high seismic anisotropy (larger than 5%) with the foliation plane plunging ~20 degrees steeper than the plate interface. This is consistent with crystallographic preferred orientation developed in S-C mylonites, and the talc could be pervasive in the transition zone where the slow slip events occur [*Song and Kim*, 2012b]. The influence of the pore pressure on seismic velocities is however expected to diminish with depth and is unlikely to be significant at lower oceanic crustal depths where the porosity is extremely low [*Christensen*, 1984].

[30] The presence of the thin low velocity layer, which we interpret to be a low strength layer (previously defined as low viscosity channel [*Manea and Gurnis*, 2007; *Hebert et al.*, 2009]), completely decouples the subducting plate from the overriding plate in the flat slab region [*Manea and Gurnis*, 2007] and may act as a slip plane for the slow slip events within a region from Acapulco to a point 100 km to the north [*Larson et al.*, 2007; *Kostoglodov et al.*, 2010; *Vergnolle et al.*, 2010; *Radiguet et al.*, 2011]. Numerical experiments by *Manea and Gurnis* [2007] showed that such a layer facilitates the evolution of subduction with a normal configuration into one with a flat portion. Plate decoupling may explain the lack of compression within the overriding plate in the last 20 Ma based on the tectonic and magmatic episodes in central Mexico [*Nieto-Samaniego et al.*, 2006; *Morán-Zenteno et al.*, 2007] regardless of the complete flat subduction geometry at shallow depth of ~45 km. Also, recent GPS observations [*Franco et al.*, 2005] and GPS data inversion of the 2001 aseismic slow slip event [*Iglesias et al.*, 2004] suggested weak couplings in the flat segment in central Mexico. *Song et al.* [2009] reported that the spatial extent of the anomalously low-velocity layer (corresponding to high pore fluid pressure layer) coincides well with the region close to the coast, where slow slip is well documented. The low-strength layer is observed along the entire length of the horizontal slab from the seismogenic zone at the trench to the point where the slab descends steeply into the mantle [*Pérez-Campos et al.*, 2008; *Kim et al.*, 2010]. Although much smaller RF conversions at the top and bottom of the oceanic crust (compared to the amplitudes near the coast) continue much deeper than the vertical extent of our migrated image (Figure 6a) [*Kim et al.*, 2012], the bottom interface of the oceanic crust cannot be traced from the migration because of the lower frequency range in the data and resolution limit [*Rondenay et al.*, 2005; *Rondenay*, 2009; *MacKenzie et al.*, 2010]. According to *MacKenzie et al.* [2010], for a layer with a dip of 60–70 degrees at 150 km depth, the resolution limit is calculated to be 9 km for the forward scattering mode whereas the backscattered modes have zero sensitivity. Although the thickness of the oceanic crust is constrained at 7–8 by RFs [*Pérez-Campos et al.*, 2008; *Kim et al.*, 2010] and at 5–7 km at the trench by seismic refraction [*Shor and Fisher*, 1961], we do not expect to determine the thickness of the steeply dipping oceanic crust based on this resolution estimate.

4.2. Partial Melt Feature Underneath the Volcanic Arc

[31] The generation and migration of aqueous fluids and melts are key to understanding the origin of volcanism and fundamental processes occurring within the mantle wedge. Previous studies have

interpreted partial melt features or presence of aqueous fluids below the arc in the mid-crust in various regions using teleseismic RFs (e.g., Iceland [*Darbyshire et al.*, 2000]), Rayleigh wave dispersion (e.g., Himalaya [*Caldwell et al.*, 2009]), and magnetotelluric (MT) data (e.g., Mexico [*Jording et al.*, 2000; *Jödicke et al.*, 2006]).

[32] The seismic image underneath the TMVB in central Mexico shows a negative discontinuity in the mantle wedge at a depth of 65–75 km, which spans horizontally beneath the arc (Figure 6a). We note that the amplitudes of this feature in the migrated image (Figure 6a) appear to be quite weak compared to the RF amplitudes (Figures 6d and S5) because of the high depth-dependent weighting scheme on lower frequency Pds phase (Figure 2c), which is suggested to be insensitive to the horizontal structure in the 2-D GRT method [*Rondenay*, 2009]. The migrated images may not resolve such structural complexities in highly heterogeneous media such as the mantle wedge because the method assumes a one-dimensional structure to migrate arrival times of the converted phases over a two-dimensional vertical projection. Multiple scattering may also contaminate the image in such complex environments, which the 2-D GRT may not properly handle. Also, we may have a possible cross-mode contamination in the Ppds phase (Figure 2d), as briefly discussed in section 3.3. Nevertheless, this negative discontinuity at the depth of 65–75 km in the mantle wedge is a robust feature and correlates to the strong conversions also seen in RFs (Figures 6d and S5), and thus we mainly focus on the RFs to interpret this feature.

[33] Strong negative (blue) RF amplitudes are present at around 6.5–8 s after P arrival at 0 s underneath the volcanic arc, TMVB (see the converted amplitudes in yellow shaded box in Figure 6d). The velocity reduction is estimated to be ~18–20% based on the RF amplitudes. This negative discontinuity is not a seismic multiple of the shallower interface beneath the arc (for instance, the partial melting feature at ~20 km depth due to magmatic activity in the TMVB) because of the absence of its multiple (see Figure S5). Similarly, the RF seismograms, filtered at 3 s, include negative arrivals at the similar depth in mantle wedge, computed from a permanent station at Mexico City, which is within the TMVB (Figure 1) [*Cruz-Atienza et al.*, 2010]. It is not clear whether these negative arrivals continue toward the northern end of the MASE transect because the resolution becomes poorer closer to the end of the profile due to insufficient sampling [*Kim et al.*, 2010]. A low-velocity anomaly in a similar depth was observed from the P wave velocity tomographic images in northeast Japan [*Zhao et al.*, 1992; *Iwamori and Zhao*, 2000] although the layer was not sharply resolved. Recently, based on the image from the 2-D GRT method, *Rondenay et al.* [2010] suggested the top of the ponded partial melt region at 60 km depth with the negative seismic velocity gradient of 10–13% in central Alaska.

[34] This horizontal feature may mark either the top of a partial melt layer (subduction-related melt) or the lithosphere-asthenosphere boundary (LAB). If the negative arrivals at the depth of 65–75 km are only present beneath the arc, we can assume that it is the top of the melt layer although the bottom of such layer is not seismically detected possibly due to small velocity or smooth temperature gradients [*Rondenay et al.*, 2010]. The release of H_2O from the hydrous minerals by slab dehydration could be in the form of a fluid phase and be a dominant source of the melt layer. The melt feature appears to be a steady state feature where the slab components continuously rise and react with the mantle wedge and produce melt. We then expect that pockets of the ponded melt accumulate at this depth beneath the active volcanoes within the TMVB, and more zone of melt accumulation (a body of multiple closely spaced melt lens rather than a homogeneous lens) forms closer to the active volcanic front at the southern end of the TMVB. Since the slab is in roll-back mode based on the evidence of trenchward migration of the volcanism [*Ferrari*, 2004; *Ferrari et al.*, 2011], the formation of the melt packets may has been laterally migrated toward the trench as the volcanic front migrates in time and space in response to variations in the convergence dynamics [*Iwamori*, 1998]. We note that it is ambiguous as to whether this melt region corresponds to locally highly attenuating region in the mantle wedge beneath the northern part of the TMVB at a depth of 80 to 120 km [*Chen and Clayton*, 2009].

[35] On the other hand, if the negative arrivals horizontally continue toward the end of the profile beyond the northern end of the TMVB, we may interpret this feature as the LAB although the depth of the LAB is quite shallow [see, e.g., *Fischer et al.*, 2010]. If the feature is the LAB, it appears that the hydrous components from the subducting slab are ascending and may be stalled at the bottom of the lithosphere prior to their ultimate ascent. In order to constrain the depth of the LAB, we need to additionally examine seismic phases such as ScS (S wave that reflects off the core-mantle boundary) reverberations that reflect off the LAB and/or S-to-P

(Sdp) converted phase that converts at the LAB [*Fischer et al.*, 2010].

5. Summary

[36] P wave coda from teleseismic events were used to invert for discontinuous variations in elastic properties beneath the dense seismic array that crosses central Mexico from Acapulco on the Pacific coast, through Mexico City, almost to Tampico on the Gulf of Mexico. Our image provides the present-day geometry of the oceanic Cocos plate subduction and orogenic processes near the trench and within the continental crust. Some key features include the very detailed images of the oceanic crust as low velocities, transitioning from shallow-to-flat to steep geometry along the transect with the slab curvature just south of the active arc (TMBV). Depressed absolute low shear wave velocities at the top interface of the subducting plate may play an important role in explaining a unique, flat slab geometry at a shallow depth (∼45 km) with very low tectonic coupling between plates. The negative discontinuity underneath the TMVB at a depth of 65–75 km with the horizontal extent of about ∼100 km may be interpreted as the top of a melt layer.

Acknowledgments

[37] We thank entire MASE team for making the data available (http://www.tectonics.caltech.edu/mase/). Y. Kim is supported by the Gordon and Betty Moore Foundation through the Tectonics Observatory at California Institute of Technology (contribution number 190) and NSF award EAR 0609707. We thank G. Abers, M. Bostock, L. MacKenzie, and S. Rondenay for discussion on imaging the steeply dipping slab. We also thank X. Pérez-Campos for providing the local seismicity data, T. Chen for providing slab contour lines for Mexico subduction zone, and T. Song and S. Straub for comments on the melt feature underneath the arc in central Mexico. Finally, we thank the Editor J. Tyburczy, Associate Editor, J. Gu, and an anonymous reviewer for helpful comments, which greatly improved the paper.

References

Abers, G. A., L. S. MacKenzie, S. Rondenay, Z. Zhang, A. G. Wech, and K. C. Creager (2009), Imaging the source region of Cascadia tremor and intermediate-depth earthquakes, *Geology*, *37*(12), 1119–1122, doi:10.1130/G30143A.1.

Audet, P., M. G. Bostock, N. I. Christensen, and S. M. Peacock (2009), Seismic evidence for overpressured subducted oceanic crust and megathrust fault sealing, *Nature*, *457*, 76–78, doi:10.1038/nature07650.

Bostock, M. G., and S. Rondenay (1999), Migration of scattered teleseismic body waves, *Geophys. J. Int.*, *137*, 732–746, doi:10.1046/j.1365-246x.1999.00813.x.

Bostock, M. G., S. Rondenay, and J. Shragge (2001), Multiparameter two-dimensional inversion of scattered teleseismic body waves: 1. Theory for oblique incidence, *J. Geophys. Res.*, *106*(B12), 30,771–30,782, doi:10.1029/2001JB000330.

Caldwell, W. B., S. L. Klemperer, S. S. Rai, and J. F. Lawrence (2009), Partial melt in the upper-middle crust of the northwest Himalaya revealed by Rayleigh wave dispersion, *Tectonophysics*, *477*, 58–65, doi:10.1016/j.tecto.2009.01.013.

Chen, T., and R. W. Clayton (2009), Seismic attenuation structure in central Mexico: Image of a focused high-attenuation zone in the mantle wedge, *J. Geophys. Res.*, *114*, B07304, doi:10.1029/2008JB005964.

Christensen, N. I. (1984), Pore pressure and oceanic crustal seismic structure, *Geophys. J. R. Astron. Soc.*, *79*, 411–423, doi:10.1111/j.1365-246X.1984.tb02232.x.

Cruz-Atienza, V. M., A. Iglesias, J. F. Pacheco, N. M. Shapiro, and S. K. Singh (2010), Crustal structure below the valley of Mexico estimated from receiver functions, *Bull. Seismol. Soc. Am.*, *100*(6), 3304–3311, doi:10.1785/0120100051.

Darbyshire, F. A., K. F. Priestley, R. S. White, R. Stefánsson, G. B. Gudmundsson, and S. S. Jakobsdóttir (2000), Crustal structure of central and northern Iceland from analysis of teleseismic receiver functions, *Geophys. J. Int.*, *143*, 163–184, doi:10.1046/j.1365-246x.2000.00224.x.

Ferrari, L. (2004), Slab detachment control on mafic volcanic pulse and mantle heterogeneity in central Mexico, *Geology*, *32*(1), 77–80, doi:10.1130/G19887.1.

Ferrari, L., M. López-Martínez, G. Aguirre-Díaz, and G. Carrasco-Núnez (1999), Space-time patterns of Cenozoic arc volcanism in central Mexico: From the Sierra Madre Occidental to the Mexican Volcanic Belt, *Geology*, *27*(4), 303–306, doi:10.1130/0091-7613(1999)027<0303:STPOCA>2.3.CO;2.

Ferrari, L., T. Orozco-Esquivel, V. Manea, and M. Manea (2011), The dynamic history of the Trans-Mexican Volcanic Belt and the Mexico Subduction zone, *Tectonophysics*, *522–523*, 122–149, doi:10.1016/j.tecto.2011.09.018.

Fischer, K. M., H. A. Ford, D. L. Abt, and C. A. Rychert (2010), The lithosphere-asthenosphere boundary, *Annu. Rev. Earth Planet. Sci.*, *38*, 551–575, doi:10.1146/annurev-earth-040809-152438.

Franco, S. I., V. Kostoglodov, K. M. Larson, V. C. Manea, M. Manea, and J. A. Santiago (2005), Propagation of the 2001–2002 silent earthquake and interplate coupling in the Oaxaca subduction zone, Mexico, *Earth Planets Space*, *57*, 973–985.

Frederiksen, A. W., and M. G. Bostock (2000), Modeling teleseismic waves in dipping anisotropic structures, *Geophys. J. Int.*, *141*, 401–412, doi:10.1046/j.1365-246x.2000.00090.x.

Gómez-Tuena, A., C. H. Langmuir, S. L. Goldstein, S. M. Straub, and F. Ortega-Gutiérrez (2007), Geochemical evidence for slab melting in the Trans-Mexican Volcanic Belt, *J. Petrol.*, *48*(3), 537–562, doi:10.1093/petrology/egl071.

Gómez-Tuena, A., L. Mori, N. E. Rinconherrera, F. Ortegagutierrez, J. Sole, and A. Iriondo (2008), The origin of a primitive trondhjemite from the Trans-Mexican volcanic belt and its implications for the construction of a modern continental arc, *Geology*, *36*, 471–474, doi:10.1130/G24687A.1.

Gorbatov, A., and Y. Fukao (2005), Tomographic search for missing link between the ancient Farallon subduction and the present Cocos subduction, *Geophys. J. Int.*, *160*, 849–854, doi:10.1111/j.1365-246X.2005.02507.x.

Gutscher, M.-A., W. Spakman, H. Bijwaard, and E. R. Engdahl (2000), Geodynamics of flat subduction: Seismicity and

tomographic constraints from the Andean margin, *Tectonics*, *19*, 814–833, doi:10.1029/1999TC001152.

Hacker, B. R., G. A. Abers, and S. M. Peacock (2003), Subduction factory 1. Theoretical mineralogy, densities, seismic wave speeds, and H_2O contents, *J. Geophys. Res.*, *108*(B1), 2029, doi:10.1029/2001JB001127.

Hebert, L. B., P. Antoshechkina, P. Asimow, and M. Gurnis (2009), Emergence of a low-viscosity channel in subduction zones through the coupling of mantle flow and thermodynamics, *Earth Planet. Sci. Lett.*, *278*, 243–256, doi:10.1016/j.epsl.2008.12.013.

Hirose, H., and K. Obara (2005), Repeating short- and long-term slow slip events with deep tremor activity around the Bungo channel region, southwest Japan, *Earth Planets Space*, *57*, 961–972.

Humphreys, E. (2009), Relation of flat subduction to magmatism and deformation in the western United States, *Mem. Geol. Soc. Am.*, *204*, 85–98, doi:10.1130/2009.1204(04).

Humphreys, E., E. Hessler, K. Dueker, E. Erslev, G. L. Farmer, and T. Atwater (2003), How Laramide-age hydration of North America by the Farallon slab controlled subsequent activity in the western U.S., in *The George A. Thompson Volume; the Lithosphere of Western North America and Its Geophysical Characterization*, *Int. Book Ser.*, vol. 7, edited by S. L. Klemperer and W. G. Ernst, pp. 524–544, Geol. Soc. of Am., Boulder, Colo.

Husker, A., and P. M. Davis (2009), Tomography and thermal state of the Cocos plate subduction beneath Mexico City, *J. Geophys. Res.*, *114*, B04306, doi:10.1029/2008JB006039.

Iglesias, A., S. K. Singh, A. Lowry, M. Santoyo, V. Kostoglodov, K. M. Larson, and S. I. Franco-Sanchez (2004), The silent earthquake of 2002 in the Guerrero seismic gap, Mexico (Mw = 7.6), Inversion of slip on the plate interface and some implications, *Geofis. Int.*, *43*, 309–317.

Iglesias, A., R. W. Clayton, X. Pérez-Campos, S. K. Singh, J. F. Pacheco, D. García, and C. Valdés-González (2010), S wave velocity structure below central Mexico using high-resolution surface wave tomography, *J. Geophys. Res.*, *115*, B06307, doi:10.1029/2009JB006332.

Iwamori, H. (1998), Transportation of H_2O and melting in subduction zones, *Earth Planet. Sci. Lett.*, *160*, 65–80, doi:10.1016/S0012-821X(98)00080-6.

Iwamori, H., and D. Zhao (2000), Melting and seismic structure beneath the northeast Japan arc, *Geophys. Res. Lett.*, *27*(3), 425–428, doi:10.1029/1999GL010917.

Jödicke, H., A. Jording, L. Ferrari, J. Arzate, K. Mezger, and L. Rüpke (2006), Fluid release from the subducted Cocos plate and partial melting of the crust deduced from magnetotelluric studies in southern Mexico: Implications for the generation of volcanism and subduction dynamics, *J. Geophys. Res.*, *111*, B08102, doi:10.1029/2005JB003739.

Jording, A., L. Ferrari, J. Arzate, and H. Jödicke (2000), Crustal variations and terrane boundaries in southern Mexico as imaged by magnetotelluric transfer functions, *Tectonophysics*, *327*, 1–13.

Kay, S. M., and C. Mpodozis (2002), Magmatism as a probe to the Neogene shallowing of the Nazca plate beneath the modern Chilean flat-slab, *J. South Am. Earth Sci.*, *15*, 39–57, doi:10.1016/S0895-9811(02)00005-6.

Kennett, B. L. N., and E. R. Engdahl (1991), Traveltimes for global earthquake location and phase identification, *Geophys. J. Int.*, *105*, 429–465, doi:10.1111/j.1365-246X.1991.tb06724.x.

Kikuchi, M., and H. Kanamori (1982), Inversion of complex body waves, *Bull. Seismol. Soc. Am.*, *71*, 491–506.

Kim, Y., R. W. Clayton, and J. M. Jackson (2010), The geometry and seismic properties of the subducting Cocos plate in central Mexico, *J. Geophys. Res.*, *115*, B06310, doi:10.1029/2009JB006942.

Kim, Y., R. W. Clayton, and F. Keppie (2011), Evidence of a collision between the Yucatán Block and Mexico in the Miocene, *Geophys. J. Int.*, *187*, 989–1000, doi:10.1111/j.1365-246X.2011.05191.x.

Kim, Y., R. W. Clayton, and J. M. Jackson (2012), Distribution of hydrous minerals in the subduction system beneath Mexico, *Earth Planet. Sci. Lett.*, doi:10.1016/j.epsl.2012.06.001, in press.

Kodaira, S., T. Iidaka, A. Kato, J. Park, T. Iwasaki, and Y. Kaneda (2004), High pore fluid pressure may cause silent slip in the Nankai Trough, *Science*, *304*, 1295–1298, doi:10.1126/science.1096535.

Kostoglodov, V., A. Husker, N. M. Shapiro, J. S. Payero, M. Campillo, N. Cotte, and R. Clayton (2010), The 2006 slow slip event and nonvolcanic tremor in the Mexican subduction zone, *Geophys. Res. Lett.*, *37*, L24301, doi:10.1029/2010GL045424.

Langston, C. A. (1979), Structure under Mount Rainier, Washington, inferred from teleseismic body waves, *J. Geophys. Res.*, *84*(B9), 4749–4762, doi:10.1029/JB084iB09p04749.

Larson, K., V. Kostoglodov, S. Miyazaki, and J. A. S. Santiago (2007), The 2006 aseismic slow slip event in Guerrero, Mexico: New results from GPS, *Geophys. Res. Lett.*, *34*, L13309, doi:10.1029/2007GL029912.

Ligorria, J. P., and C. J. Ammon (1999), Iterative deconvolution and receiver function estimation, *Bull. Seismol. Soc. Am.*, *89*, 19–36.

Lonsdale, P. (2005), Creation of the Cocos and Nazca plates by fission of the Farallon plate, *Tectonophysics*, *404*, 237–264, doi:10.1016/j.tecto.2005.05.011.

MacKenzie, L. S., G. A. Abers, S. Rondenay, and K. M. Fischer (2010), Imaging a steeply dipping subducting slab in Southern Central America, *Earth Planet. Sci. Lett.*, *296*, 459–468, doi:10.1016/j.epsl.2010.05.033.

Manea, V., and M. Gurnis (2007), Subduction zone evolution and low viscosity wedges and channels, *Earth Planet. Sci. Lett.*, *264*, 22–45, doi:10.1016/j.epsl.2007.08.030.

Melgar, D., and X. Pérez-Campos (2011), Imaging the Moho and subducted oceanic crust at the isthmus of Tehuantepec, Mexico, from receiver functions, *Pure Appl. Geophys.*, *168*, 1449–1460, doi:10.1007/s00024-010-0199-5.

Morán-Zenteno, D. J., M. Cerca, and J. D. Keppie (2007), The Cenozoic tectonic and magmatic evolution of southwestern Mexico: Advances and problem interpretation, in *Geology of Mexico, Celebrating the Centenary of the Geological Society of Mexico*, edited by S. A. Alaniz-Alvarez and Á. F. Nieto-Samanieto, *Spec. Pap. Geol. Soc. Am.*, *422*, 71–91.

Nieto-Samaniego, A. F., A. S. Alaniz-Alvarez, G. Silva-Romo, M. H. Eguiza-Castro, and C. Mendoza-Rosales (2006), Latest Cretaceous to Miocene deformation events in the eastern Sierra Madre del Sur, Mexico, inferred from the geometry and age of major structures, *Geol. Soc. Am. Bull.*, *118*, 238–252, doi:10.1130/B25730.1.

Pardo, M., and G. Suárez (1995), Shape of the subducted Rivera and Cocos plates in southern Mexico, seismic and tectonic implications, *J. Geophys. Res.*, *100*, 12,357–12,373, doi:10.1029/95JB00919.

Peacock, S. M., N. I. Christensen, M. G. Bostock, and P. Audet (2011), High pore pressures and porosity at 35 km depth in the Cascadia subduction zone, *Geology*, *39*(5), 471–474, doi:10.1130/G31649.1.

Pearce, F. D., S. Rondenay, M. Sachpazi, M. Charalampakis, and L. H. Royden (2012), Seismic investigation of the transition from continental to oceanic subduction along the western Hellenic Subduction Zone, *J. Geophys. Res.*, doi:10.1029/2011JB009023, in press.

Pérez-Campos, X., Y. Kim, A. Husker, P. M. Davis, R. W. Clayton, A. Iglesias, J. F. Pacheco, S. K. Singh, V. C. Manea, and M. Gurnis (2008), Horizontal subduction and truncation of the Cocos Plate beneath central Mexico, *Geophys. Res. Lett.*, *35*, L18303, doi:10.1029/2008GL035127.

Radiguet, M., F. Cotton, M. Vergnolle, M. Campillo, B. Valette, V. Kostoglodov, and V. Cotte (2011), Spatial and temporal evolution of a long term slow slip event: The 2006 Guerrero Slow Slip Event, *Geophys. J. Int.*, *184*, 816–828, doi:10.1111/j.1365-246X.2010.04866.x.

Rondenay, S. (2009), Upper mantle imaging with array recordings of converted and scattered teleseismic waves, *Surv. Geophys.*, *30*, 377–405, doi:10.1007/s10712-009-9071-5.

Rondenay, S., M. G. Bostock, and J. Shragge (2001), Multiparameter two-dimensional inversion of scattered teleseismic body waves, 3. Application to the Cascadia 1993 data set, *J. Geophys. Res.*, *106*(B12), 30,795–30,807, doi:10.1029/2000JB000039.

Rondenay, S., M. G. Bostock, and K. M. Fischer (2005), Multichannel inversion of scattered teleseismic body waves: Practical considerations and applicability, in *Seismic Earth: Array Analysis of Broadband Seismograms*, *Geophys. Monogr. Ser.*, vol. 157, edited by A. Levander and G. Nolet, pp. 187–203, AGU, Washington, D. C., doi:10.1029/157GM12.

Rondenay, S., G. A. Abers, and P. E. van Keken (2008), Seismic imaging of subduction zone metamorphism, *Geology*, *36*, 275–278, doi:10.1130/G24112A.1.

Rondenay, S., L. G. J. Montési, and G. A. Abers (2010), New geophysical insight into the origin of the Denali volcanic gap, *Geophys. J. Int.*, *182*, 613–630, doi:10.1111/j.1365-246X.2010.04659.x.

Rubinstein, J. L., D. R. Shelly, and W. L. Ellsworth (2010), Non-volcanic tremor: A window into the roots of fault zones, in *New Frontiers in Integrated Solid Earth Sciences*, edited by S. Cloetingh and J. Negendank, pp. 287–314, Springer, Dordrecht, Netherlands.

Schaaf, P., J. Stimac, C. Siebe, and J. L. Macias (2005), Geochemical evidence for mantle origin and crustal processes in volcanic rocks from popocatepetl and surrounding monogenetic volcanoes, central Mexico, *J. Petrol.*, *46*(6), 1243–1282, doi:10.1093/petrology/egi015.

Shor, G. G., Jr., and R. L. Fisher (1961), Middle America trench: Seismic refraction studies, *Geol. Soc. Am. Bull.*, *72*, 721–730, doi:10.1130/0016-7606(1961)72[721:MATSS]2.0.CO;2.

Shragge, J., M. Bostock, and S. Rondenay (2001), Multiparameter two-dimensional inversion of scattered teleseismic body waves: 2. Numerical examples, *J. Geophys. Res.*, *106*(B12), 30,783–30,793, doi:10.1029/2001JB000326.

Skinner, S. M., and R. W. Clayton (2010), An evaluation of proposed mechanisms of slab flattening in central Mexico, *Pure Appl. Geophys.*, *168*, 1461–1474, doi:10.1007/s00024-010-0200-3.

Song, T.-R., and Y. Kim (2012a), Anisotropic uppermost mantle in young subducted slab underplating central Mexico, *Nat. Geosci.*, *5*, 55–59, doi:10.1038/ngeo1342.

Song, T.-R. A., and Y. Kim (2012b), Localized seismic anisotropy associated with long-term slow-slip events beneath southern Mexico, *Geophys. Res. Lett.*, *39*, L09308, doi:10.1029/2012GL051324.

Song, T.-R. A., D. V. Helmberger, M. R. Brudzinski, R. W. Clayton, P. Davis, X. Pérez-Campos, and S. K. Singh (2009), Subducting slab ultra-slow velocity layer conincident with silent earthquake in southern Mexico, *Science*, *324*, 502–506, doi:10.1126/science.1167595.

Straub, S. M., A. B. LaGatta, A. L. Martin-Del Pozzo, and C. H. Langmuir (2008), Evidence from high Ni olivines for a hybridized peridotite/pyroxenite source for orogenic andesites from the central Mexican Volcanic Belt, *Geochem. Geophys. Geosyst.*, *9*, Q03007, doi:10.1029/2007GC001583.

Straub, S. M., A. Gomez-Tuena, F. M. Suart, G. F. Zellmer, R. Espinasa-Perena, Y. Cai, and Y. Iizuka (2011), Formation of hybrid arc andesites beneath thick continental crust, *Earth Planet. Sci. Lett.*, *303*, 337–347, doi:10.1016/j.epsl.2011.01.013.

Suarez, G., J. P. Ligorria, and L. Ponce (1992), Preliminary crustal structure of the coast of Guerrero, Mexico, using the minimum apparent velocity of refracted waves, *Geofis. Int.*, *31*, 247–252.

Suckale, J., S. Rondenay, M. Sachpazi, M. Charalampakis, A. Hosa, and L. H. Royden (2009), High-resolution seismic imaging of the western Hellenic subduction zone using teleseismic scattered waves, *Geophys. J. Int.*, *178*(2), 775–791, doi:10.1111/j.1365-246X.2009.04170.x.

Ulrych, T. J., M. D. Sacchi, and S. L. M. Freire (1999), Eigenimage processing of seismic sections, in *Covariance Analysis of Seismic Signal Processing*. *Geophys. Dev. Ser.*, vol. 8, edited by R. L. Kirlin and W. J. Done, pp. 241–274, Soc. Expl. Geophys., Tulsa, doi:10.1190/1.9781560802037.ch12.

Valdes-Gonzalez, C., and R. P. Meyer (1996), Seismic structure between the Pacific coast and Mexico City from the Petatlan earthquake (Ms = 7.6) aftershocks, *Geofis. Int.*, *35*, 4377–4401.

VanDecar, J. C., and R. S. Crosson (1990), Determination of teleseismic relative phase arrival times using multi-channel cross-correlation and least-squares, *Bull. Seismol. Soc. Am.*, *80*, 150–169.

Vergnolle, M., A. Walpersdorf, V. Kostoglodov, P. Tregoning, J. A. Santiago, N. Cotte, and S. I. Franco (2010), Slow slip events in Mexico revised from the processing of 11 year GPS observations, *J. Geophys. Res.*, *115*, B08403, doi:10.1029/2009JB006852.

Wallace, P., and I. Carmichael (1999), Quaternary volcanism near the Valley of Mexico: Implications for subduction zone magmatism and the effects of crustal thickness variations on primitive magma compositions, *Contrib. Mineral. Petrol.*, *135*, 291–314, doi:10.1007/s004100050513.

Wortel, R., and S. Cloetingh (1981), On the origin of the Cocos-Nazca spreading center, *Geology*, *9*, 425–430, doi:10.1130/0091-7613(1981)9<425:OTOOTC>2.0.CO;2.

Zhao, D., A. Hasegawa, and S. Horiuchi (1992), Tomographic imaging of P and S wave velocity structure beneath northeastern Japan, *J. Geophys. Res.*, *97*, 19,909–19,928, doi:10.1029/92JB00603.